

Toolbox

Correlation of 4Pi and Electron Microscopy to Study Transport Through Single Golgi Stacks in Living Cells with Super Resolution

Giuseppe Perinetti^{1,2,*}, Tobias Müller^{3,†},
Alexander Spaar¹, Roman Polishchuk¹,
Alberto Luini¹ and Alexander Egner^{3,4,*}

¹Department of Cell Biology and Oncology, Consorzio Mario Negri Sud, Santa Maria Imbaro (CH), Italy

²Department of Biomedicine, University of Trieste, Trieste, Italy

³Department of NanoBiophotonics, Max Planck Institute for Biophysical Chemistry, Am Fassberg 11, 37077 Göttingen, Germany

⁴DFG Research Center for the Molecular Physiology of the Brain (CMPB), Göttingen, Germany

*Corresponding author: Giuseppe Perinetti, G.Perinetti@fmc.units.it or Alexander Egner, aegner@gwdg.de

†These authors contributed equally to this work.

Two problems have hampered the use of light microscopy for structural studies of cellular organelles for a long time: the limited resolution and the difficulty of obtaining true structural boundaries from complex intensity curves. The advent of modern high-resolution light microscopy techniques and their combination with objective image segmentation now provide us with the means to bridge the gap between light and electron microscopy in cell biology applications. In this study, we provide the first comparative correlative analysis of three-dimensional structures obtained by 4Pi microscopy and segmented by a zero-crossing procedure with those of transmission electron microscopy (TEM). The distribution within the cisternae of isolated Golgi stacks of the cargo protein procollagen 3 was mapped by both 4Pi microscopy and TEM for a detailed comparative analysis of their imaging capabilities. A high correlation was seen for the structures, indicating the particular accuracy of the 4Pi microscopy. Furthermore, for the first time, transport of a cargo molecule (vesicular stomatitis virus G protein-pEGFP) through individual Golgi stacks (labeled by galactosyl transferase-venus-YFP) was visualized by 4Pi microscopy. Following the procedures validated by the correlative analysis, our transport experiments show that (i) VSVG-pEGFP rapidly enter/exit individual Golgi stacks, (ii) VSVG-pEGFP never fills the GalT-venusYFP compartments completely and (iii) the GalT-venusYFP compartment volume increases upon VSVG-pEGFP arrival. This morphological evidence supports some previous TEM-based observations of intra-Golgi transport of VSVG-pEGFP and provides new insights toward a better understanding of protein progression across Golgi stacks. Our study

thus demonstrates the general applicability of super-resolution fluorescence microscopy, coupled with the zero-crossing segmentation procedure, for structural studies of suborganelle protein distributions under living cell conditions.

Key words: 3D reconstruction, confocal/4Pi/electron/correlative microscopy, intra-Golgi transport, threshold, zero-crossing

Received 21 January 2008, revised and accepted for publication 27 December 2008, uncorrected manuscript published online 3 January 2009, published online 19 February 2009

In cell biology, the interdependency of structure and function is of fundamental importance, as is evident at all levels of tissue and cell organization. This begins with the external and internal morphologies of the various cell types that reflect their specialized functions within tissues and continues down to the cellular organelles, like the mitochondrion and the Golgi complex, that separate the many consecutive steps of enzymatic reactions through intricate, well-defined, sub-cellular compartmentalization. Finally, there are the structures of the biomolecules themselves that directly define the function of any given cell type.

The applicability of microscopy for functional/structural studies is unquestionable. From the multitude of techniques available, fluorescence microscopy and transmission electron microscopy (TEM) are the most commonly used. TEM has superior resolution in the nanometer range and provides information on the surrounding membrane structures in addition to those containing the specific label. Apart from being a far less demanding and time-consuming technique, fluorescence microscopy benefits from the ability to work under living cell conditions. This is particularly useful for the study of processes like intracellular trafficking. In addition, a fluorescent label provides a clearer representation of the overall distribution of a protein than immunogold labeling. Therefore, in any direct comparison with TEM, the major drawback of fluorescence microscopy is its limited resolution. Furthermore, the determination of organelle boundaries from light microscopy images also necessitates image segmentation, which is commonly achieved by applying somewhat arbitrary thresholds in a procedure that can produce unreliable structural boundaries.

The resolution of standard confocal fluorescence microscopy is limited by the diffraction of light to about 200 nm laterally and about 500 nm axially (1). Even in combination, confocal microscopy and TEM are not sufficiently powerful tools to provide us with a full understanding of many morphofunctional events, such as protein transport, vesicle fusion and subcompartmental enzyme localization (2,3).

The poor spatial resolution in light microscopy has significantly hampered biological studies on intracellular trafficking. For instance, despite a century of study of the Golgi complex, the question of how cargo crosses this organelle remains unclear. The main reasons for this lack of a clear understanding of intra-Golgi transport is the extreme structural complexity of this organelle (4), which can only be fully resolved by TEM. However, with the advent of super-resolution fluorescence microscopy technologies (5,6), the gap in resolution between light microscopy and TEM is becoming narrower, making it now possible to address many previously unanswerable questions.

Microscopy methods like 4Pi (7), I5M (8), STED (9) and RESOLFT (10) sharpen the focal spot, while imaging schemes like PALM (11), STORM (12), FPALM (13) and PALMIRA (14) rely on single-molecule switching and localization. Another technique, known as SIM, is based on structured illumination (15). However, only 4Pi microscopy combines most of the characteristics needed for studying intracellular trafficking. It provides optical sectioning and achieves a three-dimensional (3D) resolution in the 100-nm range inside whole living cells (16), it allows the use of fluorescent proteins as markers for complex 3D structures in living cell conditions (17) and its imaging speed is comparable to that of modern confocal microscopes. Very recent investigations with commercially available 4Pi microscopes have revealed the potential for the study of single protein complexes and the cellular nanomachinery in general (18) or of mitochondrial network morphology relative to oxidative phosphorylation events (19). However, these studies have been on fixed cells mounted in glycerol medium, and they have not explored the full potential of the new technology on live cell imaging. Moreover, the reconstructed 3D structures and the subsequent morphometric analyses have been performed using manually adjusted standard isosurface threshold image segmentation, however with no proof of its reliability.

Therefore, this study examines to what extent 4Pi microscopy can be used to at least partially bridge the gap between light microscopy and TEM, without losing the ability to work in 3D with living cells, and it is combined with an objective image segmentation procedure. Ultimately, we address the question relating to the circumstances and extent under which light microscopy can be used for analyses that have previously been carried out only with TEM. To this end, we present here the first comparative correlative 3D analysis of super-resolution light microscopy and TEM, as applied to protein distribu-

tion at a suborganelle level, thereby characterizing the resolving power of a 4Pi microscope. By adapting and combining the technique of correlative light-electron microscopy (CLEM) (20) with 4Pi microscopy (hereafter called 4Pi-CLEM), this has allowed us to record highly resolved images of individual intracellular structures by 4Pi microscopy and to analyze exactly the same structures under TEM using 3D reconstruction procedures.

We have thus compared standard intensity thresholding as it is used routinely in fluorescence microscopy with the automated intensity-independent 'zero-crossing' segmentation procedure (21) and show that the latter is more reliable and fully objective for determining true organelle boundaries. The combination of 4Pi-CLEM with the zero-crossing image segmentation procedure has provided a striking correlation between the 3D reconstructions from 4Pi microscopy and the corresponding TEM data.

Finally, by using this approach, as validated in the above correlative analysis, we have recorded for the first time the passage of the temperature-sensitive VSVG-pEGFP through individual Golgi stacks, labeled as GalT-venusYFP, in living mammalian cells.

Results

Procollagen-3-pEGFP-filled Golgi compartments as the structural reference for 4Pi-CLEM

Obtaining 3D images of a single structure by two methods as different as confocal/4Pi microscopy and TEM is in itself a demanding task. To compare them in a reliable and significant way necessitates the use of a sample that meets the demands of both methods of image acquisition and, most importantly, that provides highly characteristic, easily identifiable structural elements. We have therefore used the Golgi complex when filled with a fluorescent tag on a carrier molecule. The Golgi complex in mammalian cells is composed of a ribbon of multiple stacks of cisternae (easily recognizable in thin sections) that are connected by the non-compact tubular-reticular zones (22,23). However, the entire Golgi ribbon is too complex for CLEM analysis because of its large size (up to tens of microns). Thus, we took advantage of the microtubule-depolymerizing drug nocodazole that causes the Golgi ribbon to be fragmented into separate, but functional, Golgi stacks (24). A typical isolated Golgi stack comprises a number of flat sheets of cisternae that can extend for up to a micron laterally (25). While this is a suitable size range for CLEM (20), the cisternae of individual stacks are only 20–30 nm thick and are separated by an intercisternal space of similar dimension (22,23). As such, the Golgi stack still remains a difficult object for the intended structural comparison in 3D because a single cisterna would be below the resolution limit of 4Pi microscopy. We have therefore profited from a specific property of the Golgi complex, whereby the cisternae can become considerably enlarged to accommodate certain

large proteins. Our fluorescence carrier here is thus procollagen (PC) aggregates, which consist of rod-like PC monomers of about 300 nm in length and 1.5 nm in diameter, laterally clustered into a roughly 150 nm thick aggregate (3). The inclusion of PC in the cisterna lumen leads to the formation of saccular distensions of the same dimensions, which are often located at the lateral ends of the cisternae (26). These structures are well below the axial resolution limit of confocal microscopy but should be easily recognizable in 4Pi microscopy and TEM images. They therefore provided an ideal target for this comparative analysis of 3D reconstructions obtained by the parallel application of the CLEM procedure to 4Pi microscopy and TEM.

The filling cargo and fluorescent probe were provided by PC type 3 fused with an EGFP tag (PC3-pEGFP), which was expressed in BHK cells. The synchronization of PC3-pEGFP transport that was required to control its filling of the Golgi stack was performed using a combination treatment of dipyrindyl and a standard 40°C temperature protein-traffic block, as detailed in Supplementary Methods and shown in Figure S1. Furthermore, to simplify the structures to be recorded, the formation of single Golgi stacks from the Golgi ribbon was induced by treating these cells with 33 μM nocodazole for 1 h (during the PC3-pEGFP release at 32°C) before they were fixed (Supplementary Methods and Figure S1). Under these conditions, the Golgi components redistribute from their central position into separate Golgi stacks that are scattered throughout the cytoplasm (25,27). Note that this treatment has also been shown not to interfere with the normal transport activity of the Golgi (25).

Microscopy recordings

The workflow of the 4Pi-CLEM technique is shown in Figure 1, and examples from recordings from the individual

microscopy techniques are shown in Figures S2 and S4. Initially, a wide-field microscope was used to preselect a cell that showed clearly identifiable isolated Golgi stacks. To aid in the later identification, we recorded the fluorescence (Figure S2A) and differential interference contrast (DIC) (Figure S2B) images of the cell. Next, a confocal 3D sequence of the Golgi stack of interest was acquired (Figure S2D), prior to the 4Pi microscopy recording that completed the fluorescence imaging part of the protocol (Figure S2E).

The specimen was then processed for immuno-TEM, and after the cell had again been identified, an initial low-magnification (1050 \times) analysis was performed to provide a direct comparison between the DIC microscopy and the TEM imaging (Figure S2B,C). A series of multiple images at medium magnification (20 500 \times) was then recorded for each slice to ascertain the identification of the selected Golgi stack (Figure S2F, GS1). The relative positions with respect to two other reference Golgi stacks were also taken into account during this process (Figures S2D–F, RG1, RG2). To further confirm the data obtained, the same procedure was carried out with a second cell (Figure S4), although without the initial confocal microscopy recording; here, a single reference Golgi stack and a larger and structurally more complex Golgi stack were used (Figure S4, RG, GS2, respectively).

3D reconstruction of the TEM data

In both cases, once the Golgi stacks had been correctly identified as indicated above, a series of high-magnification (43 500 \times) images of the organelles was recorded (Figures S3 and S5). In reconstructing the Golgi stacks, the structural elements were categorized as follows: (i) *cisternae*, showing the typical elongated shape; (ii) enlarged *saccular distensions*, as PC3-pEGFP-positive compartments that were continuous with the cisternae; and (iii) *carriers*, as

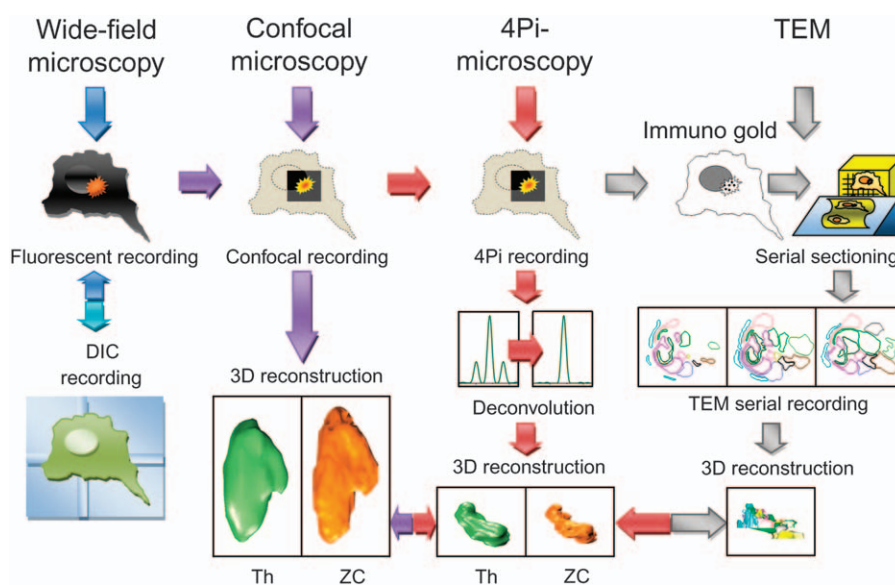


Figure 1: Overview of the 4Pi-CLEM technique. Details of all procedures are reported in the text. Th, threshold intensity procedure. ZC, zero-crossing procedure.

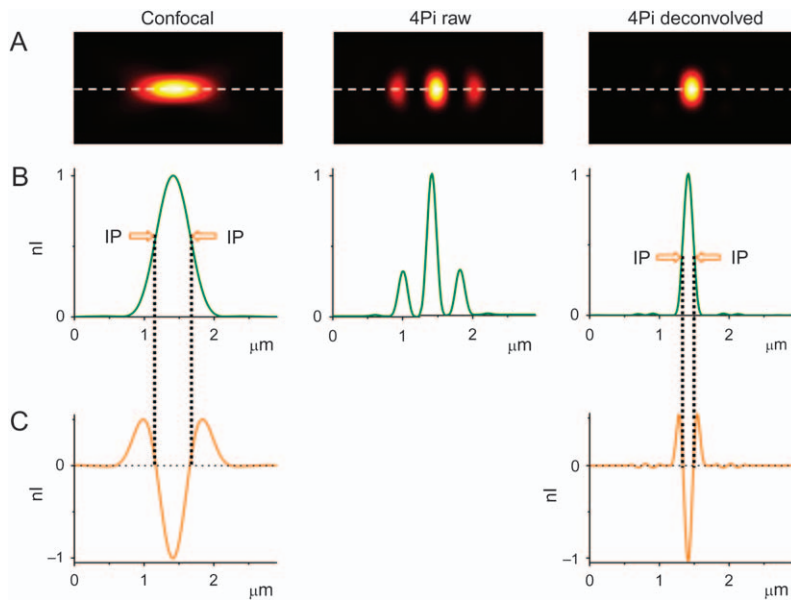


Figure 2: Simulated point spread functions and their corresponding curves with the zero-crossing procedure for the confocal and 4Pi microscopy recordings. A) Simulated microscopy point images. B) Simulated curves of the point spread functions detected along the dotted white lines in (A). C) Simulated curves obtained from the point spread function curves for the zero-crossing procedure. IP, inflection point (of maximum slope); n , normalized intensity.

PC3-pEGFP-positive compartments with no apparent continuity with the Golgi stack. These carriers were also included in the reconstruction because of their proximity to the body of the Golgi stack, which renders them indistinguishable at the 4Pi microscopy level of resolution.

3D reconstruction of the confocal and 4Pi microscopy data

A standard feature of 4Pi microscopy recordings is the formation of side lobes along the z-axis (5). As illustrated in Figure 2, these were initially removed using a deconvolution procedure (28) that was applied prior to the 3D reconstruction of the final images (see also *Materials and Methods*). In the next step, the confocal and 4Pi microscopy data were used for the 3D reconstruction by two separate image segmentation procedures: (i) a standard threshold intensity procedure (29) and (ii) an intensity-independent, edge detection technique that is known as zero crossing (21).

By definition, the threshold intensity procedure produces an edge in two dimensions or an isosurface in 3D, which corresponds to arbitrarily chosen threshold values. Here, by computing and optimizing the degree of correlation between the various thresholds of the 4Pi microscopy and the TEM reconstructions, the optimal threshold values were separately obtained for the two Golgi stacks selected for the full analysis. To achieve this, the intersection of the $k1$ and $k2$ Manders coefficient curves [representing, effectively, the fraction of the volume of the 4Pi reconstruction ($k1$) and of the TEM reconstruction ($k2$) that is colocalized (30) (Supplementary Methods for details)] was used to extrapolate the optimal threshold levels for the 4Pi recordings (see Figure 3A,B for Golgi stack 1 and Golgi

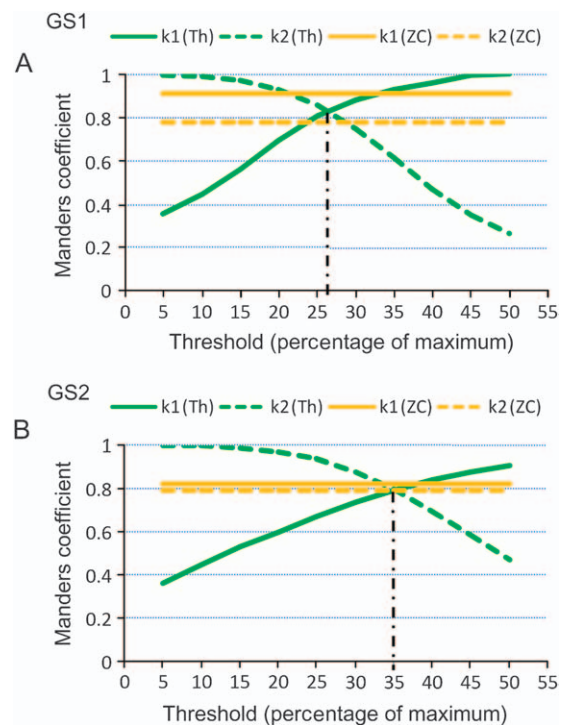


Figure 3: Manders coefficients for the 4Pi microscopy and TEM recordings. GS1, Golgi stack 1; GS2, Golgi stack 2. For the 3D reconstructions using the threshold intensity procedure, the crossing of the $k1$ (Th) and $k2$ (Th) (green) curves provides the best Manders coefficients, which correspond to threshold levels of 26% (A) and 35% (B) of the maximum intensities of the signals for Golgi stacks 1 and 2, respectively. The Manders coefficients represent the fraction of the volume of the 4Pi reconstruction ($k1$) and of the TEM reconstruction ($k2$) that is colocalized. Th, threshold intensity procedure; ZC, zero-crossing procedure.

stack 2, respectively). This resulted in an intensity threshold of 35% of the maximum intensity for Golgi stack 1 using confocal microscopy (data not shown), and with the values of 26% and 35% chosen for Golgi stacks 1 and 2, respectively, using 4Pi microscopy (Figure 3A,B). The calculation of Manders coefficients of confocal/TEM structures was omitted because of the evident mismatch of resolution along the optical axis (Figure 4, top), giving little meaning to any comparison.

However, determining the optimum intensity threshold was only possible because we had the information from the TEM data at hand. In a purely light microscopy-based study, such as a time-lapse experiment, this *a priori* information would not be available. Moreover, intensity thresholding is likely to introduce errors when applied to complex intensity distributions. Therefore, the more objective intensity-independent edge detection technique, which is known as the zero-crossing procedure, was applied to provide a further reconstruction of the 4Pi-CLEM data of the Golgi stacks (21,29) (Figure 2B,C). In this zero-crossing procedure, the edges of the structural elements

are assumed to correspond to the inflection points of the intensity functions (Figure 2B). At these positions, the absolute values of the slope are maximal, and therefore, the first derivative shows a maximum and the Laplacian (the second derivative) changes sign, i.e. crosses the zero. These 'zero crossings' serve as the tool for the recognition of edges (in 2D) and surfaces (in 3D). The main advantage of this method over the threshold intensity procedure is its invariance upon variations in intensity, which thus produces reliable surfaces of objects with complex intensity distributions without the need to enhance the brighter, or suppress the darker, parts. Assuming that the cisternal distensions and carriers are fully filled by PC3-pEGFP, the edges that are defined by the zero-crossing procedure will correspond to the membranes of the compartment boundary, providing structures that are ideally suited for comparison with the outlines gained from TEM recordings.

With this zero-crossing procedure applied to the 4Pi microscopy recordings of the two Golgi stacks under consideration, the k_1 and k_2 Manders coefficients (which are independent of the maximum intensities) provided

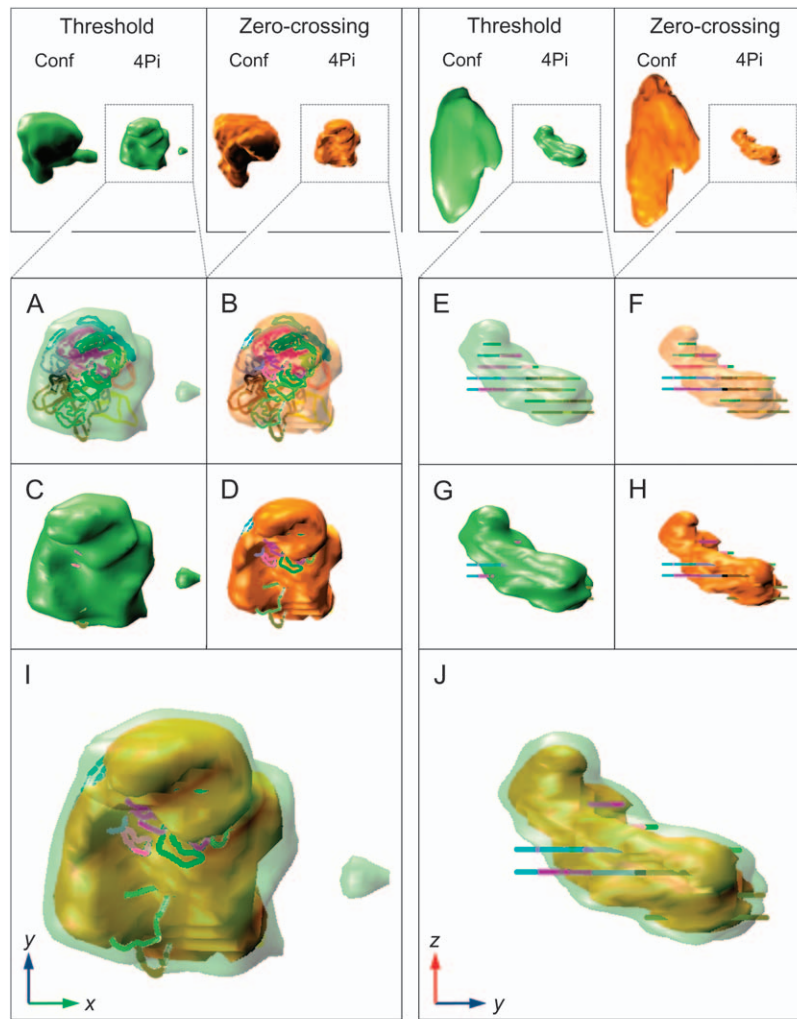


Figure 4: Confocal fluorescence and 4Pi microscopy and TEM 3D reconstructions of Golgi stack 1. A–J) Merged 4Pi microscopy (as compartments) and TEM (as lines) 3D reconstructions. The individual threshold intensity and zero-crossing 4Pi reconstructions are shown in both transparent A, B, E and F) and opaque C, D, G and H) modes. I and J) Overlays for the threshold intensity and zero-crossing 4Pi 3D reconstructions (transparent and opaque, respectively) with the TEM 3D reconstruction. For clarity, individual cisternae and carriers are outlined in different colors, which are maintained between this figure and Figure S3. Bar, 1250 nm (top panels); 500 nm (A–H); 250 nm (I and J). Threshold, threshold intensity procedure; zero-crossing, zero-crossing procedure. The threshold levels for the maximum intensities were set at 35% for the confocal microscopy and 26% for the 4Pi microscopy.

values that were very close to each other: $k_1 = 0.91$ and $k_2 = 0.78$ for Golgi stack 1 (Figure 3A) and $k_1 = 0.81$ and $k_2 = 0.79$ for Golgi stack 2 (Figure 3B). This confirms the very good correlation with the TEM recordings that was already evident by visual comparison (Videos S1–S4, respectively). Additionally, these k_1 and k_2 values are higher than those provided by the intersection of the curves for the threshold-based segmentation procedure, indicating higher total overlap and thus superior definition of organelle boundaries.

Overlapped 3D reconstructions

The most important goals of these reconstructions were to define the 3D overlap of the data from the confocal/4Pi microscopy and TEM recordings to ultimately demonstrate the high resolution that is achievable through the 4Pi technology and to determine the reliability of the zero-crossing procedure for image segmentation. This was accomplished by using the VISUAL MOLECULAR DYNAMICS (VMD) software in which the TEM data were correctly interfaced using a dedicated MATLAB routine. From the reconstructions shown in Figures 4 and 5 and in Videos S1–S4, it can immediately be seen that the structures derived from the 4Pi microscopy recordings show strikingly more detail than those obtained by standard confocal microscopy. As would be expected, the fourfold to fivefold resolution enhancement of 4Pi microscopy compared with confocal microscopy leads to significant improvements in the structural reconstruction along the z-axis (Figures 4 and 5).

Within each of the 4Pi microscopy recordings, good overlap with the TEM-derived structures was evident for both of the Golgi stacks examined (Figure 4, Golgi stack 1; Figure 5, Golgi stack 2). Analyses of the correlation of the 4Pi microscopy structures with those from the TEM showed discrepancies between these two techniques that were in the range of 100–200 nm, and thus within the order of magnitude of the resolution difference between 4Pi microscopy and TEM, as would be expected. Generally, the 3D reconstructions from the 4Pi microscopy were slightly larger when compared with those from the corresponding TEM data (Figures 4 and 5); this is an effect that probably arises from the slight shrinkage that inevitably occurs during sample preparation for TEM. Additionally, a slight overestimation of the Golgi stack volumes in 4Pi reconstructions might occur because of the presence of minor structural details below the microscope resolution limit. At the same time, some of the TEM structures (mainly for Golgi stack 1) extend outside the 4Pi microscopy reconstructions (Figure 4). However, these are cisternae that have the classical flat and elongated structures, and as such, they are too small to contain the 300 nm long PC3-pEGF molecules, in contrast to the distensions filled by the EGFP tag. These same cisternae did not show any gold labeling in the nonoverlapping areas from the TEM, in parallel with the lack of fluorescent tag in the 4Pi microscopy reconstructions (for Golgi stack 1, compare Figure 4 with Figure S3D,E). However, the distensions that were positive for the EGFP tag in TEM images always appeared

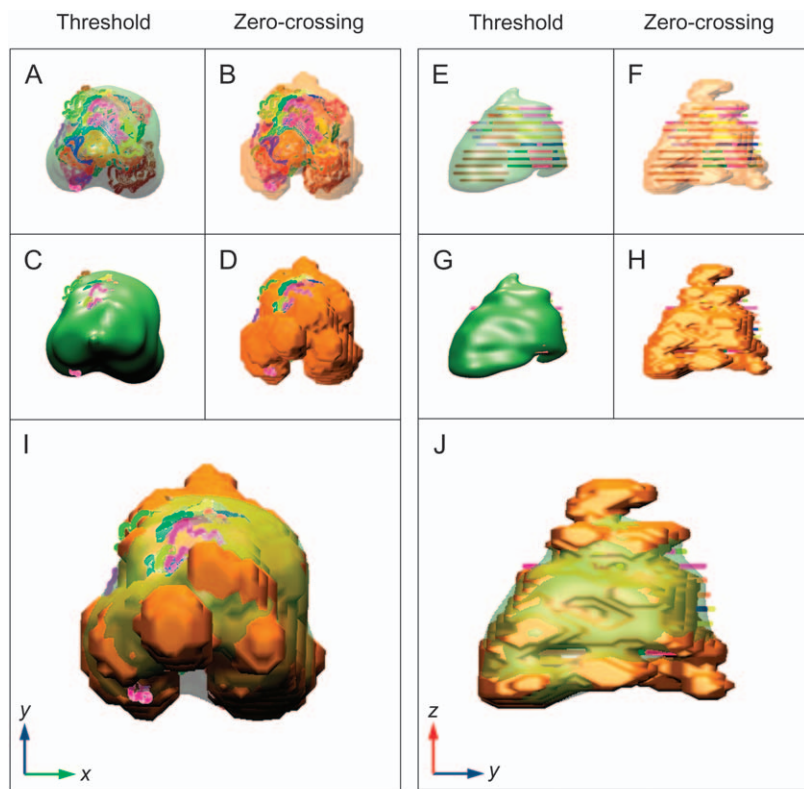


Figure 5: 4Pi microscopy and TEM 3D reconstructions of Golgi stack 2. A–J) Merged 4Pi microscopy (as compartments) and TEM (as lines) 3D reconstructions. The individual threshold intensity and zero-crossing 4Pi reconstructions are shown both in the transparent A, B, E and F) and opaque C, D, G and H) modes. I and J) Overlays for the threshold intensity and zero-crossing 4Pi 3D reconstructions (transparent and opaque, respectively) with the TEM 3D reconstruction. For clarity, individual cisternae and carriers are outlined in different colors, which are maintained between this figure and Figure S5. Bar, 1 μm (A–H); 500 nm (I and J). Threshold, threshold intensity procedure; zero-crossing, zero-crossing procedure. The threshold level for the maximum intensity was set at 35%.

to be almost completely within the 4Pi microscopy reconstructions (Figures 4 and 5, Figures S3 and S5 and Videos S1 and S3 for Golgi stacks 1 and 2, respectively).

This is also reflected in the Manders coefficients of the structures segmented by the zero-crossing procedure (Figure 3A). The notable difference between k_1 and k_2 for the zero-crossing-segmented Golgi stack 1 (Figure 3A), and the Manders coefficients that are generally large, at up to 0.9, but not exactly 1.0, might be explained by the inherent differences between the two imaging methods. In the TEM reconstruction, differential protein distributions within the different structural elements are not taken into account, whereas in the 4Pi reconstruction, they are directly mapped as an intensity distribution. Thus, the overlap between the two reconstructions is high but will not be perfect.

Also of note is that for the standard thresholding, the intersections of the Manders coefficient curves for Golgi stacks 1 and 2 provided different threshold settings (26 and 35%, respectively), demonstrating the poor repeatability of the threshold method and thus again the superiority of the zero-crossing procedure.

Analysis of VSVG-pEGFP passage through the GalT-venusYFP Golgi compartment in living cells

We then used similar approaches in living cells to determine how transmembrane secretory cargo traverses the Golgi complex. We coexpressed a transmembrane cargo protein and a Golgi-resident enzyme fused with fluorescent tags. Two-color 4Pi microscopy recordings (31), deconvolution (17) and zero-crossing procedures were applied as described in the above correlative analyses. Thereby, the passage of this cargo through the Golgi complex was recorded in three dimensions in a time-lapse manner.

In particular, the vesicular stomatitis virus G protein (VSVG) and the *trans*-Golgi protein galactosyl transferase (GalT) (32), fused with the pEGFP and venusYFP tags, respectively, were coexpressed in COS7 cells (Figure S6). Specifically, VSVG is a secretory cargo, as the G protein of the ts045 mutant of vesicular stomatitis virus (33), and it can be accumulated in the endoplasmic reticulum (ER) at 40°C and released into the secretory pathway in a synchronous pulse by shifting the temperature to 32°C (34). However, the correct localization of GalT within the Golgi stack of cisternae is determined by its transmembrane domain, which has been used here instead of the wild-type GalT (17,27). In any case, the *trans*-Golgi localization of the GalT-venusYFP was confirmed by immuno-TEM, as detailed in the Supplementary Methods and shown in Figure S7.

As for the correlative analyses, the transport of VSVG-pEGFP was followed through single Golgi stacks of cisternae induced by treating these cells with nocodazole for 3 h before the temperature shift. Moreover, at the same time as the cargo was released from the ER, 100 $\mu\text{g}/\text{mL}$

cycloheximide was added to the medium to reduce protein synthesis and the secretory load (25). The cell viability, cargo synchronization efficacy and normal rate of transport under the experimental 4Pi microscopy recording conditions had been previously demonstrated, as detailed in the Supplementary Methods.

Separated nocodazole-induced Golgi stacks were used for these experiments because previous studies had demonstrated that Golgi stacks represent a simple and reliable model to investigate transport through the Golgi complex [see *Discussion* in Trucco et al. (25)] and because their relatively small size affords substantial gains in speed of acquisition, which also results in reduction of specimen bleaching. With the settings used in the present investigation, ~ 1.5 min was necessary for a full 3D recording of a volume that was ~ 3.5 μm thick. Because the *trans*-Golgi and the VSVG-pEGFP compartments in the Golgi stacks analyzed herein showed maximum dimensions of ~ 1 – 1.5 μm , they required ~ 30 – 40 seconds for the recordings. Therefore, the 4Pi microscopy allowed the four-dimensional (4D) recording of up to nine consecutive time-points before the bleaching of the structures precluded further reliable imaging.

By 4Pi microscopy recording, the following parameters were monitored for each time-point: (i) distance between the VSVG-pEGFP and GalT-venusYFP fluorescent signal centers of gravity (as defined in the Supplementary Methods), (ii) weighted colocalization of the GalT-venusYFP compartment(s) with the VSVG-pEGFP compartment(s), (iii) volume of the GalT-venusYFP compartment(s) and (iv) shape of the GalT-venusYFP compartment and the presence of small structures resembling vesicles. A total of 13 Golgi stacks from different cells were analyzed, covering a range of ~ 4 – 35 min after the temperature shift, and 2 (from the same cell, referred to as Golgi stack 3 and Golgi stack 4) are reported here as representative examples of the VSVG-pEGFP entrance into and exit from the GalT-venusYFP compartment, respectively. Galleries of the 3D recordings of these two Golgi stacks are shown in Figure 6, with the quantitative outcomes shown in Figure 7.

The time required for the VSVG-pEGFP to enter the GalT-venusYFP compartment in different Golgi stacks was not the same in all the cases, ranging from ~ 4 to ~ 8 min after removal of the 40°C temperature block (time 0) (not recorded). For instance, Golgi stacks 3 and 4 (which belonged to the same cell) showed variability in their times of entrance (and exit) of the VSVG-pEGFP cargo into (and from) the GalT-venusYFP compartment (Figure 7). After the temperature shift, the centers of gravity of VSVG-pEGFP and of GalT-venusYFP (which are usually at least 300 nm away from each other before transport through the Golgi begins) started to become closer (Figure 7A), indicating that the VSVG-pEGFP bulk moved toward the GalT-venusYFP compartment. Later, vice versa, the gravity centers of the two fluorophores started separating again, suggesting that

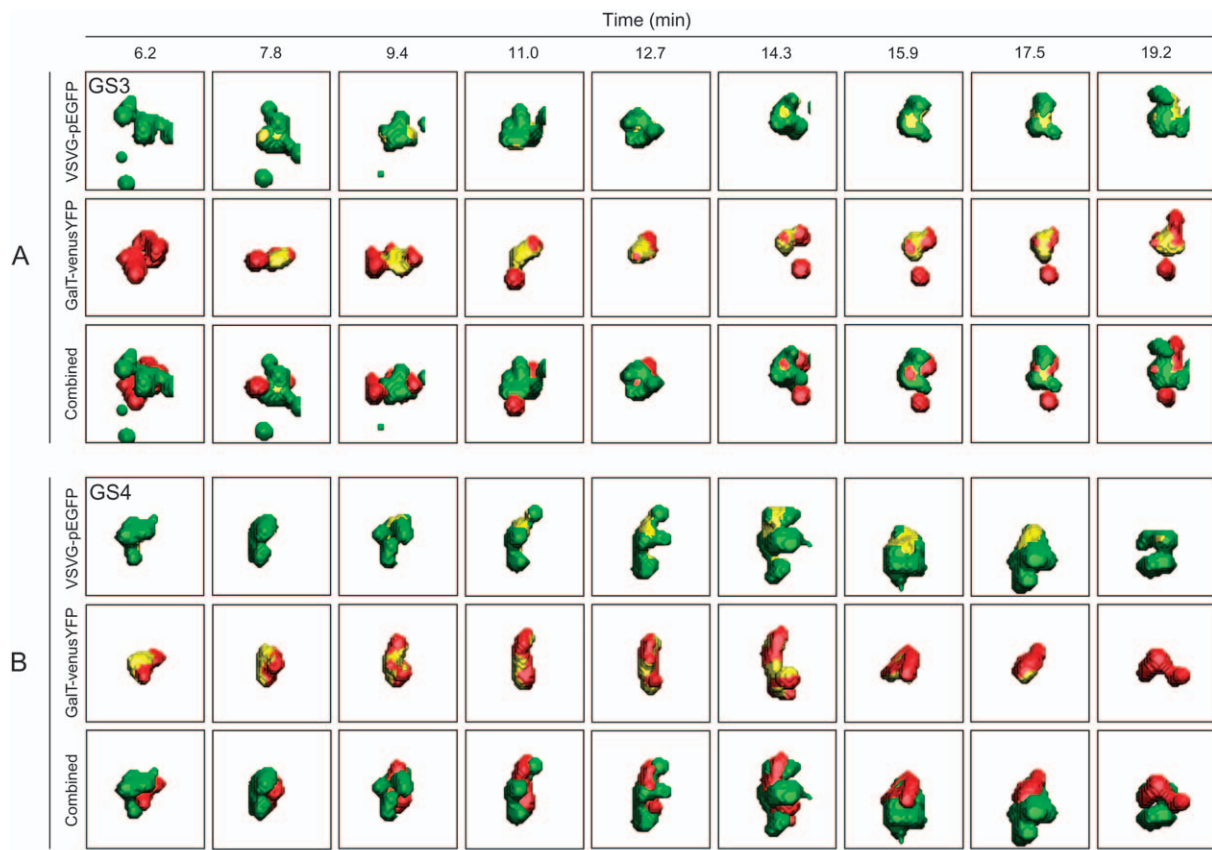


Figure 6: Time-lapse 4Pi microscopy recordings of Golgi stacks 3 and 4. GS3, Golgi stack 3; GS4, Golgi stack 4. For the 3D reconstructions and calculation, the deconvolution and the zero-crossing segmentation procedures have been used as reported in the correlative analysis. The time (in min) of the consecutive recordings is as indicated (6.2–19.2 min). Green, VSVG-pEGFP, red, GalT-venusYFP, yellow, colocalizing areas for the Golgi stack 3 (A) and 4 (B). Bar, 300 nm.

VSVG-pEGFP was leaving the GalT-venusYFP compartment (Figure 7B). Notably, small structures resembling peri-Golgi vesicles that were positive for either VSVG-pEGFP or GalT-venusYFP were not seen. This indicates that either such vesicles are absent or that they are close enough to the stack as to become indistinguishable from the Golgi mass at the 4Pi microscopy level of resolution.

The relationships between the gravity center parameter and the GalT-venusYFP compartment volume and shape are also of interest as these also underwent changes during the passage of VSVG-pEGFP (Figure 6). In particular, as the distance between the centers of gravity dropped below ~ 130 nm (presumably corresponding with the entrance of VSVG-pEGFP into the stack; Figure 7A), the GalT-venusYFP volume increased and, vice versa, it decreased during exit of the VSVG-pEGFP from the stack (stack 4, Figure 7B). This can be explained by the significant addition of volume to the GalT-venusYFP compartment at the moment when VSVG-pEGFP membranes were integrated into the stack. Notably, these volume changes appear to be related to the presence (rather than the degree) of colocalization (Figure 7).

One of the unexpected findings was the incomplete filling of the GalT-venusYFP compartment by VSVG-pEGFP (i.e. partial colocalization), which lasted for the entire process of passage through the Golgi (Figure 7, and other Golgi stacks not shown). Thus, even when the GalT-venusYFP colocalization with VSVG-pEGFP achieved maximum values, portions of the GalT-venusYFP compartment appeared to be devoid of cargo. By decomposing the 3D reconstructions of both the VSVG-pEGFP and the GalT-venusYFP compartments at each time-point in their single 2D slices, the colocalization areas appear to have no preferential distribution on the GalT-venusYFP compartment, and in most of the cases, a single overlapping area was seen per time-point (data not shown).

Discussion

By implementing the 4Pi-CLEM technique, we have shown that super-resolution fluorescence microscopy can indeed be reliably applied to the recording of complex-shaped intracellular compartments. Although the phase changes induced by variations in the refractive indices between the

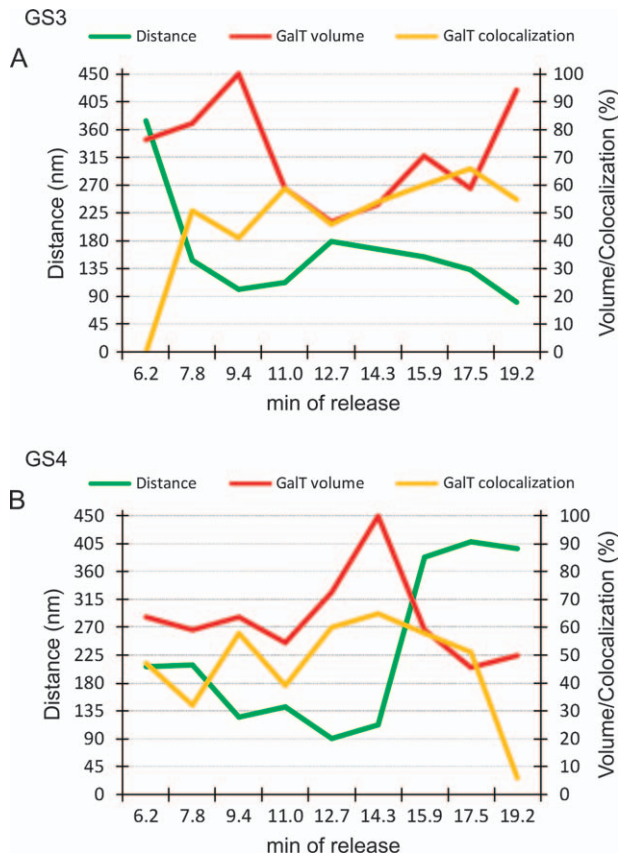


Figure 7: Quantitative analysis of VSVG-pEGFP passage through the GalT-venusYFP compartment in Golgi stacks 3 and 4 (entrance and exit, respectively). GS3, Golgi stack 3; GS4, Golgi stack 4. For the 3D reconstructions and calculation, the deconvolution and the zero-crossing segmentation procedures have been used as reported in the correlative analysis. The entrance and exit of the VSVG-pEGFP to and from the GalT-venusYFP compartment are shown in GS3 (A) and GS4 (B), respectively. Distance, distance between the centers of gravity of the pEGFP and venusYFP channels (VSVG and GalT, respectively); GalT volume, normalized GalT-venusYFP compartment volume changes over time; GalT colocalization, normalized degree of weighted GalT-venusYFP compartment colocalizing with the VSVG-pEGFP compartment. GalT volume and colocalization are normalized to the corresponding highest values and presented as percentages.

aqueous medium and the cell interior can alter the structure of the point spread function (see *Materials and Methods*) (35,36), this did not significantly affect the reliability of the 4Pi microscopy. Indeed, even in close proximity to the nucleus (as for Golgi stack 2), the nonhomogenous distribution of the refractive indices is weak enough, so as not to alter the phase relation between the focused illumination wave fronts, producing reliable deconvolution outcomes in the 3D analyses. Furthermore, the zero-crossing segmentation procedure was tested successfully for the 3D reconstructions of these two Golgi stacks, showing that it can be used to overcome the limits of the structural uncertainties that are introduced by the standard threshold

intensity procedure, which is a method based on a subjective choice. Moreover, as a biological application, the procedure tested by the correlative analysis has been used to follow the passage of VSVG-pEGFP through the *trans*-Golgi complex (as labeled with GalT-venusYFP) in a time-lapse manner. We have here recorded the passage of cargo through the Golgi stacks for the first time by 4Pi microscopy in living cells.

This technique thus promises to be a powerful method that is in principle extendable to all types of fluorescence microscopy for 3D analysis as well as for 2D analysis. In addition to purely morphological studies, other analyses, such as colocalization of two or three fluorescent markers, which is widely used in studying trafficking events, can also greatly benefit from this zero-crossing procedure because it is objective and independent from the absolute and local intensity maxima. In time-lapse experiments under live cell conditions, this procedure can also be expected to yield reconstructions that are less altered by the level of progressive bleaching that can follow repeated measurements.

In the direct comparisons shown here, a number of aspects indicate the superiority of the zero-crossing procedure over that of standard thresholding. The structures that we have reconstructed by zero-crossing generally lead to greater correlation with the TEM-derived structures, which is also reflected in the higher Manders coefficients (Figures 3A,B). In the standard thresholding procedure, it is assumed that the true surface of the 3D reconstructed structure corresponds to an isosurface of constant fluorescent intensity equal to the thresholding value, a condition that may not reflect the reality, especially for larger organelles, such as Golgi stack 2, with its complex structural organization. However, in the case of the simpler and smaller Golgi stack 1, thresholding can also be quite precise, although it must be noted that the threshold values were set *a posteriori*, following the computing of the overlap with the TEM-derived structures. Moreover, the standard threshold intensity procedure can induce further errors as the distribution of the fluorescent tag is fitted to a TEM structure that does not contain any information about the protein concentration or distribution. The noticeable differences between the threshold intensity values computed for the Golgi stack reconstructions also clearly show the low reliability of this fixed threshold segmentation procedure. This limitation is of particular importance when there is the need for objective segmentation of multiple structural elements in one image or of objects with a highly complex intensity distribution.

However, despite the zero-crossing procedure being a powerful method that has seen widespread application in spectrometry and fluorescence spectrophotometry (21), this procedure has to date seen only very limited, if any, use in fluorescence microscopy as applied to cellular studies (37). Indeed, no previous study has investigated the relia-

bility of this procedure in depth. Thus, through the use of correlative microscopy, the present study has demonstrated the reliability of the zero-crossing procedure, and ultimately, we would propose to extend the application of this procedure to all fluorescence microscopy techniques.

Through our comparative analysis of the structures provided by 4Pi-CLEM, we have also shown that the combination of super-resolution microscopy with this objective, intensity-independent, zero-crossing image segmentation technique provides a tool for investigations into highly resolved organelle structures that is of unprecedented power. The usability of this combination of methods is enhanced even further by introducing the ability to work under live cell conditions.

Any study of cellular structures with details of interest in the range of 100–500 nm, thus below the limit of confocal axial resolution (1), can benefit from this method. Currently, 1–2 seconds per image slice are needed, making 3D recordings of small structures available in steps of 1 or 2 min. Although there are cellular processes that can already be visualized this way, as reported here for the transport of VSVG-pEGFP through a Golgi stack, the method can be speeded up by more than an order of magnitude by implementing a faster scanner (e.g. a Nipkow scanner). Nevertheless, several advantages of 4Pi microscopy over other methods for the investigation of the living cell Golgi can already be appreciated. For example, 4Pi microscopy revealed details of the Golgi dynamics upon the arrival of cargo (such as enlargement of the GalT-venusYFP compartment) that could be detected in the past only by TEM (25).

The mechanism(s) by which cargoes traverse the Golgi complex is still controversial (2). Several models have been proposed, including (i) the vesicular shuttle model (38), (ii) the cisternal maturation model in different variants (25,26,39,40) and (iii) the cargo diffusion and partitioning model within a two-phase membrane system (41). These inconsistencies arise at least partially as most of the results have been derived indirectly, that is by TEM analysis, with only a few studies based on living cells (39–42). Unfortunately, even these live cell-based studies have produced contradictory results in favor of either the cisternal maturation model (39,40) or others predicting the cisternae as stable compartments (41,42).

Although the present 4Pi recordings do not allow a full kinetic analysis, the mode of exit of the VSVG-PEGFP from Golgi stack 4 (Figure 6, 17.5 and 19.2 min time-points) appears to be rapid in the range of ~1–2 min. This rapid exit might fit the view of the exponential kinetics of exit of the cargo from the Golgi that was proposed recently (41). In contrast, the linear exit of the cargo from the Golgi complex, as would be expected for the cisternal progression/maturation model, would last significantly longer than 2 min (25,41). However, the different protocols used in the

VSVG-pEGFP synchronization could also explain apparent inconsistencies in the present findings and those previously reported by immune-TEM by Trucco et al. (25).

The unexpected incomplete colocalization seen in the present investigation fits what has been previously reported (41,42). Interestingly, the segregation of the cargo and Golgi enzyme has been explained by the formation of a cargo/processing domain, which would remain connected with the Golgi complex to allow the correct biochemical reactions to take place. However, these previous investigations were based on standard confocal microscopy, whose resolution limit might have hampered the detection of important details. We show here that although remaining partially segregated from the VSVG-pEGFP compartment, the GalT-venusYFP compartment reversibly increases its volume upon the arrival of the cargo (Figure 7). This increase can be explained by the arrival of membranes from the ER upon the temperature shift to 32°C. Interestingly, a previous TEM analysis showed an increase in length and number of Golgi cisternae upon the arrival of the cargo (25). It is thus possible that the membranes derived from cargo-containing carriers coming from the ER into the Golgi do not easily mix with the enzyme-containing Golgi membranes and that these enzymes only transiently diffuse into this cargo compartment to allow glycosylation.

However, we did not find the side-by-side type of segregation of the VSVG-pEGFP compartment with respect to the GalT-venusYFP that would be expected according to these previous observations (41,42). Indeed, we observed a random spatial relationship between these two compartments (sometimes with one compartment in the apparent center of the other), which fits better the immuno-TEM data showing that cargo labeling can be found throughout the Golgi cisternae (25,26). Further dual time-lapse experiments made with 4Pi microscopy by labeling both *cis*- and *trans*-Golgi compartments during a traffic wave would provide further insight into the cargo passage through the Golgi complex.

Finally, small structures that might represent Golgi vesicles, either positive for VSVG-pEGFP or positive for GalT-venusYFP, were not seen during the present recordings (Figure 6). Because our 4Pi microscopy settings would only detect vesicles further than 100–150 nm from the rims of the cisternae (16), our data simply indicate that enzyme- or cargo-containing vesicles are not detected beyond this distance during trafficking.

Conclusions

In this study, 4Pi microscopy has been pushed to the limit of its spatial resolution to verify that it is a powerful enough technique to image 3D substructures of trafficking organelles. Also, this study is the first to characterize to what

extent the domains of applicability of light and electron microscopy overlap and to use an intensity-independent zero-crossing segmentation procedure to produce accurate 3D reconstructions of the Golgi complex.

In our view, considering that the time resolution of this technique can be further increased by the use of faster scanners and that the setup for carrying out traffic synchronization experiments can be further optimized, the 4Pi microscopy approach has the potential to become a powerful tool for the study of trafficking organelles in living cells at unprecedented 3D resolution.

Materials and Methods

Antibodies, DNA and other reagents

Unless otherwise indicated, all chemicals and reagents were obtained from previously described sources (16). Dipyrindyl was from Sigma-Aldrich (no. 630-S), nocodazole was from CalBiochem (no. 487928; Merck KGaA), cycloheximide was from CalBiochem (no. 239763; Merck KGaA), the rabbit polyclonal antibody to EGFP was from Abcam (no. ab6722), the nanogold-conjugated Fab fragments of anti-rabbit immunoglobulin G and Gold Enhancer were from Nanoprobes (no. 2004), the pEGFP-C1 vector was from DB Bioscience Clontech and the *Bgl*II and *Hind*III restriction enzymes were from Roche.

Full-length PC type 3 alpha-1 chain (COL3A1, GenBank accession no. X14420) was amplified by polymerase chain reaction (PCR) using the forward primer of 5'-GCGAGATCTCAACAGGAAGCTGTTGAAGGAGGA-3' and the reverse primer of 5'-GCGAAGCTTTTATAAAAAGCAACAGGGCCA-3'. The PCR product was then ligated in-frame with the pEGFP-C1 vector using the *Bgl*II and *Hind*III restriction sites inserted in the forward and reverse primers, respectively. Plasmid DNA was amplified from the XL1-Blue *Escherichia coli* strain using the Endotoxin-free Plasmid Kit (Qiagen).

Cell culture and treatments

BHK/COS7 cells were grown in DMEM with 4/2 mM glutamine, 10% heat-inactivated fetal calf serum, 100 U/mL penicillin and 0.1 mg/mL streptomycin at 5% CO₂ and 37°C. For DNA transfection, BHK and COS7 cells were passaged into 100-mm dishes 2 days before transfection to provide cell confluence on the day of transfection. The cells were then trypsinized and washed with PBS, and the pellet was resuspended in the DNA solution containing either 10 µg PC3-pEGFP (for the BHK transfection) or a combination of 17/1 µg of VSVG-pEGFP/GalT-venusYFP (for the COS7 cotransfection) in 400 µl cytomix (120 mM KCl, 10 mM KH₂PO₄, 10 mM MgK₂HPO₄, 2 mM EGTA, 5 mM MgCl₂, 25 mM HEPES, 0.15 mM CaCl₂, 5 mM Glutathione (GSH) and 2 mM ATP, pH 7.4). The cells were immediately electroporated using a 4-mm-path cuvette in a Gene Pulser II electroporator (Bio-Rad) (pulse, 0.220 kV; capacitance, 800/950 µF for the BHK/COS7 cells). Subsequently, the transfected BHK cells were grown on coverslips with photo-etched, numbered grids (Bellco Biotechnology), while the COS7 were grown on normal coverslips.

For the BHK cells, 24 h after electroporation, PC3-pEGFP transport was blocked in the ER for 1 h at 40°C and then released by an additional 1 h at 32°C to provide bulk flow of this cargo protein. The cells were then fixed with 4% paraformaldehyde for 15 min, immediately before the confocal and 4Pi microscopy recordings. For the COS7 cells, 6 h after electroporation, they were incubated overnight at 40°C to accumulate VSVG-pEGFP within the ER. Subsequently, VSVG-pEGFP transport was released by shifting the temperature to 32°C. Allowing for the technical manipulations of the samples (i.e. mounting the coverslips), the effective time-lapse 4Pi microscopy recording started 3–6 min after the cargo release. For

both of the cell lines, the synchronization protocols were performed and verified as reported in the Supplementary Methods and as shown in Figures S1 and S6.

Conventional wide-field and confocal microscopy

For wide-field microscopy, a Leica DM6000B microscope was used (Leica Microsystems CMS GmbH). Both DIC and fluorescence pictures were taken with 10× and 40× objectives (HCX PL Fluotar 40×/0.75 and HC PL Fluotar 10×/0.30). A GFP filter cube was used for fluorescence imaging (470/40; 500; 525/50). Confocal microscopy was performed with a Leica TCS SP5 microscope (Leica Microsystems CMS GmbH) using a 63× water immersion objective (HCX PL APO 63×/1.20), an excitation wavelength of 488 nm and a pinhole size of 1 Airy unit.

4Pi microscopy

In 4Pi microscopy, illumination by two opposing objective lenses produces a point spread function that comprises a sharp central maximum flanked in the beam directions by the lower side lobes (Figure 2). To remove these side lobes, the raw 4Pi microscopy data were deconvolved with a simple linear filter in the correlative part of this study. Because our time-lapse experiments were carried out at a lower signal-to-noise ratio, 4D recordings were deconvolved using a Richardson–Lucy algorithm (43). This enabled the recording of up to nine consecutive time-points.

Two-photon excitation of EGFP was performed at a wavelength of 890 nm, with an array of 20 4Pi foci, each with a mean power of 1.5 mW. The sample was scanned at a rate of 2 seconds per xy slice. A mode-locked Ti:sapphire laser (Mai Tai; Spectra Physics) was used for excitation, and the fluorescence was imaged onto a back-thinned cooled charge-coupled device (CCD) camera. The linear phase shift induced by the residual difference between the refractive indices of the water immersion liquid and the mounting medium [DMEM cell culture growth medium (Invitrogen), plus Dextran MW 39 400; 3.4% of total weight (Sigma)] was actively compensated for. Typical stacks comprised 100 xy images that were axially separated by 80 nm.

For two-color, 4Pi microscopy, EGFP and venusYFP were simultaneously excited at a wavelength of 890 nm. The fluorescent light from the sample was split into two channels (475–525 and 525–600 nm), which were both imaged onto the same chip of our CCD camera. As the fluorescent proteins showed a strong overlap of their emission spectra, we used linear unmixing (44) to separate the individual signals.

3D reconstructions from light microscopy data

To avoid artifacts because of residual noise, the 3D data sets were slightly presmoothed with a Gaussian filter. The threshold intensity and zero-crossing procedures were implemented in MATLAB and used for the 3D reconstruction of the Golgi stacks. For all of the zero-crossing procedures, the background pixels below 20% of the maximum point spread function intensity were cut before calculating the zero-crossing algorithm. The Manders coefficients were calculated as detailed elsewhere and in the Supplementary Methods. For visualization, the vMD software was used.

Transmission electron microscopy

Immediately after the 4Pi microscopy recordings, the cells were further fixed with 0.05% glutaraldehyde for 10 min and then permeabilized to allow the labeling of the PC3-pEGFP with the antibody sensitive to the EGFP tag. Nanogold labeling was performed and developed using the GoldEnhance protocol (Biotrend Chemikalien). Membranes were stained by applying 2% OsO₄ for 45 min. Subsequently, the samples were dehydrated and embedded in Epon-812 (Epoxy Embedding Medium Kit; Sigma-Aldrich).

After resin polymerization, the coverslips were dissolved in 40% hydrofluoric acid. The cells of interest were identified again under a stereomicroscope (Leica Microsystems CMS GmbH) using the negative imprint of the reference grid on the surface of the embedded sample and the relative positions of the surrounding cells. Subsequently, the sample was trimmed

to obtain a small pyramid with the cell of interest in the center. Sections of 80-nm thickness were collected with a metal loop (Perfect Loop; Agar), placed on slot grids covered with carbon–formvar supporting film and observed by TEM without additional staining. A Philips Technai-12 electron microscope (Philips) equipped with an ultra view CCD digital camera was used to acquire the TEM images.

3D overlap of the 4Pi-TEM reconstructions

After manual tracing of the boundary membranes of compartments positive for PC3-pEGFP in the serial TEM recordings, image files were aligned and loaded into VMD as contour lines. Finally, the 3D overlap between the 4Pi microscopy and the TEM reconstructions was performed within the VMD software. A manual alignment of the 4Pi microscopy and TEM reconstructed structures was performed by only shifting and rotating the structures along the three axes without any rescaling.

Acknowledgments

The authors are grateful to Christopher Paul Berrie, Mario Gimona and Roberto Buccione (Conorzio Mario Negri Sud) and Jaydev Jethwa (MPI for Biophysical Chemistry) for critical reading of the manuscript, to Andreas Schoenle (MPI for Biophysical Chemistry) for his 'IMSPECTOR' software used for image deconvolution and to Jan Keller (MPI for Biophysical Chemistry) for help with the calculation of the Manders coefficients.

Supporting Information

Additional Supporting Information may be found in the online version of this article:

Figure S1: Synchronization of PC3-pEGFP transport in BHK cells. At 1 h and at 40°C block, all the PC3-pEGFP (green) is in the ER and no colocalization is seen with the Golgi marker giantin (red). Once the transport is released, the PC3-pEGFP enters the transport pathway through the Golgi complex. In particular, after 1 h of release at 32°C, colocalization of PC3-pEGFP with giantin (yellow, arrows) is evident. Confocal images, 63× magnification.

Figure S2: Overview of the first cell, with the identification of Golgi stack 1. A) Wide-field fluorescent recording. B) Wide-field DIC recording. C) Low-magnification TEM recording. D and E) Confocal fluorescent and 4Pi microscopy recordings of Golgi stack 1 (GS1) and the reference Golgi stacks 1 and 2 (RG1, RG2). F) TEM recording of Golgi stack 1 (GS1) and reference Golgi stacks 1 and 2 (RG1 and RG2). The white box in (A) represents the field of view for (D and E). Bars, 25 μm (A–C); 5 μm (D and E); 500 μm (F).

Figure S3: Serial TEM recording for Golgi stack 1. Each consecutive slice, labeled from (A–H), is 80-nm thick. For every slice, the raw TEM recordings (left columns) along with those including the corresponding outlines of the reconstructed structures (right column) are shown. For clarity, individual cisternae and carriers are outlined in different colors, which are maintained between this figure and Figure 4 of the main text. Bar, 500 nm.

Figure S4: Overview of the second cell, with the identification of Golgi stack 2. A) Wide-field fluorescent recording. B) Wide-field DIC recording. C) Low-magnification TEM recording. D) 4Pi microscopy recording of Golgi stack 2 (GS2) and the reference Golgi stack (RG). E) TEM recording of Golgi stack 2 (GS2) and reference Golgi stack (RG). The white box in (A) represents the field of view for (D). Bars, 20 μm (A–C); 15 μm (D); 700 μm (E).

Figure S5: Serial TEM recording for Golgi stack 2. Each consecutive slice, labeled from (A–M), is 80-nm thick. For every slice, the raw TEM recordings (left columns) along with those including the corresponding outlines of the reconstructed structures (right column) are shown. For clarity, individual cisternae and carriers are outlined in different colors, which are maintained between this figure and Figure 5 of the main text. Bar, 500 nm.

Figure S6: VSVG-pEGFP transport synchronization in COS7 cells coexpressing GalT-venusYFP. The cells were treated as for the 4Pi microscopy transport experiment and fixed after 1 h of VSVG-pEGFP (green) release (red, GalT-venusYFP). Once the transport is released, the VSVG-pEGFP enters the transport pathway and after 60 min of release at 32°C, the arrival of VSVG-pEGFP at the plasma membrane is evident. The white box represents the field of view for the detailed merge panel. Confocal images, 63× magnification.

Figure S7: GalT-venusYFP immuno-TEM localization in the Golgi stack of COS7 cells. TEM recordings of two representative Golgi stacks immunostained for GalT-venusYFP, showing a discrete restriction of the labeling to the *trans* most cisterna(e). Bar, 250 nm.

Video S1: The 3D overlap of the 4Pi microscopy reconstruction made by the zero-crossing procedure (transparent) and the TEM recordings for Golgi stack 1.

Video S2: The 3D overlap of the 4Pi microscopy reconstruction made by the zero-crossing procedure (opaque) and the TEM recordings for Golgi stack 1.

Video S3: The 3D overlap of the 4Pi microscopy reconstruction made by the zero-crossing procedure (transparent) and the TEM recordings for Golgi stack 2.

Video S4: The 3D overlap of the 4Pi microscopy reconstruction made by the zero-crossing procedure (opaque) and the TEM recordings for Golgi stack 2.

Please note: Wiley-Blackwell are not responsible for the content or functionality of any supporting materials supplied by the authors. Any queries (other than missing material) should be directed to the corresponding author for the article.

References

- Pawley J. Handbook of Biological Confocal Microscopy. New York: Plenum; 1995.
- Mironov AA, Beznoussenko GV, Polishchuk RS, Trucco A. Intra-Golgi transport: a way to a new paradigm? *Biochim Biophys Acta* 2005;1744: 340–350.
- Bachinger HP, Morris NP, Davis JM. Thermal stability and folding of the collagen triple helix and the effects of mutations in osteogenesis imperfecta on the triple helix of type I collagen. *Am J Med Genet* 1993;45:152–162.
- Beznoussenko GV, Mironov AA. Models of intracellular transport and evolution of the Golgi complex. *Anat Rec* 2002;268:226–238.
- Hell SW. Toward fluorescence nanoscopy. *Nat Biotechnol* 2003;21: 1347–1355.
- Hell SW. Far-field optical nanoscopy. *Science* 2007;316:1153–1158.
- Hell SW. Double-scanning confocal microscope. European Patent patent 0491289. 1990.
- Gustafsson MGL, Agard DA, Sedat JW. Sevenfold improvement of axial resolution in 3D widefield microscopy using two objective lenses. *Proc SPIE* 1995;2412:147–156.

9. Hell SW, Wichmann J. Breaking the diffraction resolution limit by stimulated emission: stimulated emission depletion microscopy. *Opt Lett* 1994;19:780–782.
10. Hofmann M, Eggeling C, Jakobs S, Hell SW. Breaking the diffraction barrier in fluorescence microscopy at low light intensities by using reversibly photoswitchable proteins. *Proc Natl Acad Sci U S A* 2005;102:17565–17569.
11. Betzig E, Patterson GH, Sougrat R, Lindwasser OW, Olenych S, Bonifacino JS, Davidson MW, Lippincott-Schwartz J, Hess HF. Imaging intracellular fluorescent proteins at nanometer resolution. *Science* 2006;313:1642–1645.
12. Rust MJ, Bates M, Zhuang X. Sub-diffraction-limit imaging by stochastic optical reconstruction microscopy (STORM). *Nat Methods* 2006;3:793–796.
13. Hess ST, Girirajan TPK, Mason MD. Ultra-high resolution imaging by fluorescence photoactivation localization microscopy. *Biophys J* 2006;91:4258–4272.
14. Egner A, Geisler C, von Middendorff C, Bock H, Wenzel D, Medda R, Andresen M, Stiel AC, Jakobs S, Eggeling C, Schonle A, Hell SW. Fluorescence nanoscopy in whole cells by asynchronous localization of photoswitching emitters. *Biophys J* 2007;93:3285–3290.
15. Gustafsson MG. Surpassing the lateral resolution limit by a factor of two using structured illumination microscopy. *J Microsc* 2000;198:82–87.
16. Egner A, Jakobs S, Hell SW. Fast 100-nm resolution three-dimensional microscope reveals structural plasticity of mitochondria in live yeast. *Proc Natl Acad Sci U S A* 2002;99:3370–3375.
17. Egner A, Verrier S, Goroshkov A, Soling HD, Hell SW. 4Pi-microscopy of the Golgi apparatus in live mammalian cells. *J Struct Biol* 2004;147:70–76.
18. Hueve J, Wesselmann R, Kahms M, Peters R. 4Pi microscopy of the nuclear pore complex. *Biophys J* 2008;
19. Plecita-Hlavata L, Lessard M, Santorova J, Bewersdorf J, Jezek P. Mitochondrial oxidative phosphorylation and energetic status are reflected by morphology of mitochondrial network in INS-1E and HEP-G2 cells viewed by 4Pi microscopy. *Biochim Biophys Acta* 2008;
20. Polishchuk RS, Polishchuk EV, Marra P, Alberti S, Buccione R, Luini A, Mironov AA. Correlative light-electron microscopy reveals the tubular-saccular ultrastructure of carriers operating between Golgi apparatus and plasma membrane. *J Cell Biol* 2000;148:45–58.
21. O'Haver TC. Potential clinical applications of derivative and wavelength-modulation spectrometry. *Clin Chem* 1979;25:1548–1553.
22. Rambourg A, Clermont Y. Three-dimensional electron microscopy: structure of the Golgi apparatus. *Eur J Cell Biol* 1990;51:189–200.
23. Ladinsky MS, Mastronarde DN, McIntosh JR, Howell KE, Staehelin LA. Golgi structure in three dimensions: functional insights from the normal rat kidney cell. *J Cell Biol* 1999;144:1135–1149.
24. Lippincott-Schwartz J, Zaal KJM. Cell cycle maintenance and biogenesis of the Golgi complex. *Histochem Cell Biol* 2000;114:93–103.
25. Trucco A, Polishchuk RS, Martella O, Di Pentima A, Fusella A, Di Giandomenico D, San Pietro E, Beznoussenko GV, Polishchuk EV, Baldassarre M, Buccione R, Geerts WJ, Koster AJ, Burger KN, Mironov AA et al. Secretory traffic triggers the formation of tubular continuities across Golgi sub-compartments. *Nat Cell Biol* 2004;6:1071–1081.
26. Bonfanti L, Mironov AA Jr, Martinez-Menarguez JA, Martella O, Fusella A, Baldassarre M, Buccione R, Geuze HJ, Mironov AA, Luini A. Procollagen traverses the Golgi stack without leaving the lumen of cisternae: evidence for cisternal maturation. *Cell* 1998;95:993–1003.
27. Cole NB, Sciaky N, Marotta A, Song J, Lippincott-Schwartz J. Golgi dispersal during microtubule disruption: regeneration of Golgi stacks at peripheral endoplasmic reticulum exit sites. *Mol Biol Cell* 1996;7:631–650.
28. Schrader M, Bahlmann K, Giese G, Hell SW. 4Pi-confocal imaging in fixed biological specimens. *Biophys J* 1998;75:1659–1668.
29. Young TY, Gerbrands JJ, van Vliet LJ. Fundamentals of Image Processing. <http://www.ph.tn.tudelft.nl/Courses/FIP/noframes/fip.html>. 1995.
30. Manders EMM, Verbeek FJ, Aten JA. Measurement of co-localization of object in dual-colour confocal images. *J Microsc* 1993;169:375–382.
31. Khimich D, Nouvian R, Pujol R, Dieck ST, Egner A, Gundelfinger ED, Moser T. Hair cell synaptic ribbons are essential for synchronous auditory signalling. *Nature* 2005;434:889–894.
32. Roth J, Berger EG. Immunocytochemical localization of galactosyltransferase in HeLa cells: codistribution with thiamine pyrophosphatase in trans-Golgi cisternae. *J Cell Biol* 1982;93:223–229.
33. Gallione CJ, Rose JK. A single amino acid substitution in a hydrophobic domain causes temperature-sensitive cell-surface transport of a mutant viral glycoprotein. *J Virol* 1985;54:374–382.
34. Hirschberg K, Miller CM, Ellenberg J, Presley JF, Siggia ED, Phair RD, Lippincott-Schwartz J. Kinetic analysis of secretory protein traffic and characterization of golgi to plasma membrane transport intermediates in living cells. *J Cell Biol* 1998;143:1485–1503.
35. Egner A, Schrader M, Hell SW. Refractive index mismatch induced intensity and phase variations in fluorescence confocal, multiphoton and 4Pi-microscopy. *Opt Commun* 1998;153:211–217.
36. Blanca CM, Bewersdorf J, Hell SW. Determination of the unknown phase difference in 4Pi-confocal microscopy through the image intensity. *Opt Commun* 1998;206:281–285.
37. Raman S, Maxwell CA, Barcellos-Hoff MH, Parvin B. Geometric approach to segmentation and protein localization in cell culture assays. *J Microsc* 2007;225:22–30.
38. Palade G. Intracellular aspects of the process of protein synthesis. *Science* 1975;189:347–358.
39. Matsuura-Tokita K, Takeuchi M, Ichihara A, Mikuriya K, Nakano A. Live imaging of yeast Golgi cisternal maturation. *Nature* 2006;441:1007–1010.
40. Losev E, Reinke CA, Jellen J, Strongin DE, Bevis BJ, Glick BS. Golgi maturation visualized in living yeast. *Nature* 2006;441:1002–1006.
41. Patterson GH, Hirschberg K, Polishchuk RS, Gerlich D, Phair RD, Lippincott-Schwartz J. Transport through the Golgi apparatus by rapid partitioning within a two-phase membrane system. *Cell* 2008;133:1055–1067.
42. White J, Keller P, Stelzer EH. Spatial partitioning of secretory cargo from Golgi resident proteins in live cells. *BMC Cell Biol* 2001;2:19.
43. Richardson WH. Bayesian-based iterative method of image restoration. *J Opt Soc Am* 1972;62:55–59.
44. Zimmermann T, Rietdorf J, Pepperkok R. Spectral imaging and its applications in live cell microscopy. *FEBS Lett* 2003;546:87–92.